Subsurface Pipes Detection Using DNN-based Back Projection on GPR Data

Jinglun Feng, Liang Yang, Haiyan Wang, Yingli Tian and Jizhong Xiao
City College of New York
jfeng1@ccny.cuny.edu

Abstract

Localization and reconstruction of underground targets, the problem of estimating the position and geometry of the objects from Ground Penetration Radar (GPR), still lies at the core of non-destructive testing (NDT). In this paper, we present MigrationNet, a learning-based approach to detect and visualize subsurface objects. Compared with the existing learning-based method of GPR, our proposed approach could not only detect the hyperbola feature in the raw B-scan image but also interpret hyperbola features into the cross-section image of subsurface pipes. Furthermore, to compare the proposed method with the conventional back-projection methods for GPR data interpretation, a synthetic GPR dataset that mimics the real NDT environment is also introduced in this work. The study indicates the effectiveness of our method, it uses less GPR data for underground pipes reconstruction, produces better GPR imaging results with less computation, and shows the robustness to noise.

1. Introduction

Ground Penetration Radar (GPR) is a geophysical remote sensing method that has been widely used as a non-destructive testing (NDT) technique, thanks to its high resolution and fast detection capability. As a context of smart cities, GPR serves as a NDT tool for infrastructure applications [6, 29], it evaluates the subsurface location and condition such as concrete rebars, buried utilities and other pipe-shaped objects. [3, 4, 8, 21]. In the meanwhile, GPR could also reveal the relative size of the subsurface objects since a larger pipe-shaped object would reflect as a wider hyperbola feature in the B-scan image.

In the current practice of GPR inspection, the surveys would be performed in pre-defined straight line routes and each survey would generate a B-scan image. However, due to the difficulties of GPR signals analysis, there are two major challenges in underground objects reveal when using GPR. The first one is that GPR B-scan data still relies heavily on human efforts and experienced experts to identify because of the abstract hyperbolic feature. How to take advantages of the GPR raw data is significant in NDT. Secondly, the conventional migration methods, which aim at GPR data interpretation, are either theoretically complicated or computationally costly. An approach to design intuitive and simple migration method to interpret raw GPR data is crucial as well.

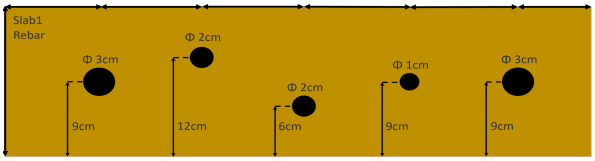

(a) Ground-Truth of a slab with 5 rebars of different size and location

(b) GPR B-scan image

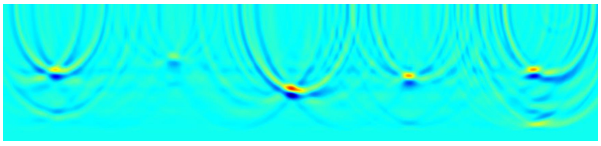

(c) Migration result of conventional back-projection method

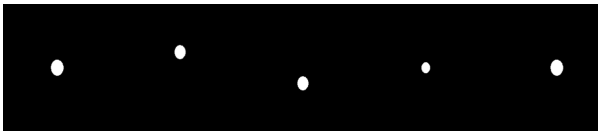

(d) Migration result of our DNN-based migration method

Figure 1. GPR imaging: a) ground truth of a slab, b) GPR B-scan image, c) migration result using conventional back projection method, d) migration result of our proposed DNN-based migration method.

Our work is inspired by the above challenges, we propose a learning-based method which mimics the migration process to reconstruct the focused subsurface targets from B-scan image in both geometry and size metric. As illustrated in Fig.1, the conventional back projection method

represents the migration result as focused target point in the energy map cannot reveal the size of the object, while our proposed DNN-based migration method can reveal both the location and size of the underground target in a binary image.

The paper is organized as follows. Section 2 introduces the related works in GPR researches while Section 3 introduces basic concepts on GPR data. In Section 4 our proposed new DNN-based migration method is discussed in details. Section 5 presents some experimental results and Section 6 concludes the paper and discusses the future work.

2. Related Works

Conventional Migration Methods Various migration methods are used to transform the unfocused raw GPR B-scan data to a focused matter which reveals the position of the objects [24]. In the 1970s, back-propagation [18] based methods such as the Kirchhoff method [28], the phase-shift method [12] and Fourier finite-difference method [7] are introduced to achieve migration. In [15,16], the authors introduced 3D migration methods by obtaining the spatial sampling of GPR measurements that is significant for the comprehension of GPR data. In this paper, the back-projection algorithm [9] is implemented for migration as a baseline method because it is widely used in industry, which will be discussed in detail in Section 3.2.

Machine Learning in Migration In addition to the many studies that have been carried out on the conventional GPR migration methods, machine learning based methods are also widely researched for automatic detection of GPR data. In [1], a Hough transform based approach on GPR signals is first proposed for underground targets detection. SVM applications in GPR studies are also widely implemented for the analysis of GPR B-scan images, [10] proposed a SVM-based method in order to classify materials of buried structures. In the meantime, [25] also proposed a SVM method for GPR images analysis which achieved an improved classification task while maintaining a low computational complexity.

Deep Learning in Migration Compared with the traditional machine learning based methods, the advantage of DNN-based method gives a better performance in terms of representing GPR images with multiple levels of abstraction. By implementing Faster R-CNN, [5,19,26,33] extract useful structures from 2D GPR raw images and use them to detect subsurface objects. [2] proposed two new CNNs to classify GPR B-scan features such as depth and dielectric information. In [20,32], DNN-based methods are also used as a solution for hyperbolic feature and real target detection. Furthermore, in order to obtain the sparse representations of GPR data, [13] proposed a dictionary learning method for better feature extraction and classification.

However, the above methods are constrained only to detection and classification on GPR B-scan image rather than interpretation of the intrinsic of GPR B-scan data. To the best of the authors knowledge, such DNN-based GPR data interpretation and migration work was rarely reported.

3. GPR Data Preliminary

In this section, we will introduce the principle of GPR scan data and demonstrate basis data processing of GPR.

3.1. GPR Scans

GPR antenna transmits a pulse of polarized high-frequency radar wave and waits for the signal to echo back – the result is called an *A-scan*. The A-scan measures the amplitudes of the electromagnetic (EM) energy and the traveled time of the reflected signal. As depicted in Fig.2, when the GPR moves on the ground over a rebar along a trajectory, it produces a series of A-scans at different positions and this ensemble of A-scans forms a B-scan, which is usually displayed in gray scale image as a hyperbola.

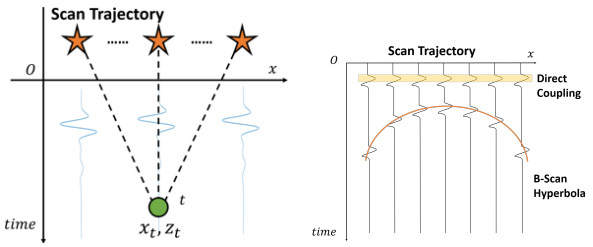

(a) Each A-scan measures amplitude of the refelcted EM wave (b) B-scan displayed in gray scale image as a hyperbola

Figure 2. An illustration of GPR working principle, (a) the star represents a GPR antenna move along straight line over a rebar that take A-scan measurement at each position; (b) the ensemble of A-scan forms a B-scan displayed as a hyperbola.

EM wave attenuates as it travels in medium and reflects when it encounters a change in material. EM wave propagates fast in materials with low dielectric, and slow down in materials with high permittivity. Since each different material has different electrical conduction properties, the amplitude and strength of the reflection will be influenced too.

3.2. Back Projection

As one of the most representative GPR imaging algorithms, back projection (BP) is a practical method widely used in industry. As we discussed in the previous section, the essence of A-scan represents amplitude of EM energy, while back projection is a process of aggregation which would convert the different amplitude of energy into a *semi-sphere* format at different depth. As illustrated in Fig.4, the brighter semi-sphere indicates the higher amplitude part in

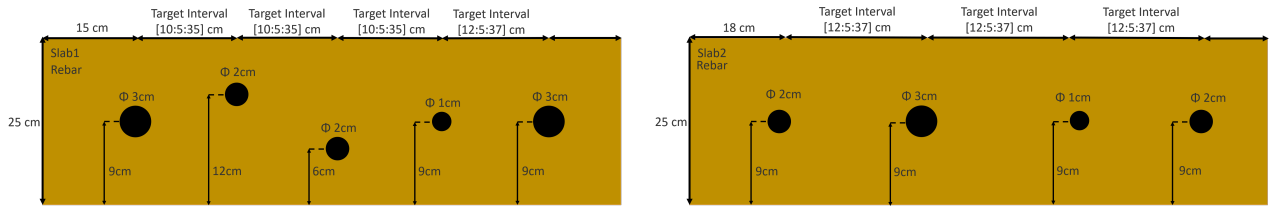

(a) Slab design with 5 PECs buried

(b) Slab design with 4 PECs buried

Figure 3. Slab design with different number of PECs and different PEC intervals.

A-scan, in the meanwhile, the radius of each semi-sphere in BP image indicates the depth of the A-scan pulse. By implementing the BP algorithm in B-scan data, the back-projected data could be represented in Equ.1 [22].

$$\forall A_q^k \in B_k,\ (x-a)^2+(y-b)^2=(a_t*t)^2,\ y<0 \quad (1)$$

where a,b represents the specific position of each A-scan measurement in a slab. $A_q^k=\{a_t|t=1,...,n_q\}$ represents the q-th A-scan measurement in k-th B-scan data, while t and a_t indicate the traveling time and amplitude of A-scan signal respectively, then n_q means the total samples in a A-scan measurements. Meanwhile, we also have $B_k=\{A_q^k|q=1,...,n_k\}$, which represents the k-th B-scan consisting of n_k A-scans.

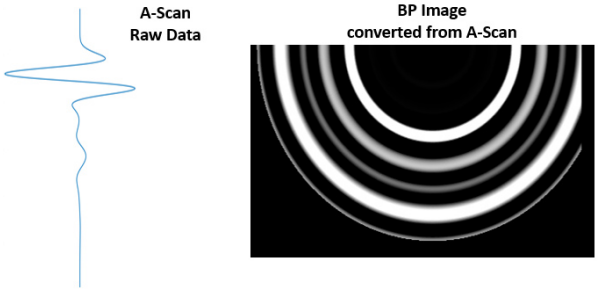

Figure 4. The implementation of BP algorithm which would convert the A-scan raw data into several semi-spheres.

3.3. GPR Migration

GPR migration aims at transferring the unfocused raw B-scan data to a focused target, a normal migration process is usually composed of the following steps:

- Take raw B-scan data as input
- Time-zero correction (adjust the response so that the time-zero corresponds to the reflection from the surface of the ground)
- Background removal (remove the direct coupling area between GPR transmitter and the ground surface)
- Back projection processing
- Hilbert transformation (filter out noise for more focused single spot of target location)

4. DNN-Based Migration

In this section, we firstly propose a synthetic GPR dataset for non-destructive testing and introduce the details of this dataset. Then, we demonstrate how we prepare the data for experiment study. At last, the architecture of our proposed DNN-based migration process is illustrated in details.

4.1. Dataset Setup

gprMax Data Generation

Since it is hard to get the ground truth of underground objects from real environment in non-destructive testing, by taking advantages of gprMax [31], we build a synthetic testing environment which simulates the real NDT condition.

For those objects need to be evaluated in real underground environment, most of them are pipe-shaped with a round cross section, for example, rebars, utilities and PVC pipes. Our simulated environment mimics this property and involves pipe-shaped objects with different location as well as the size. Notice that all of the simulated objects have a round cross section. Furthermore, in order to match the data collection in commercial GPR, our synthetic GPR B-scan dataset are finally generated along the line route.

Specifically, we build 12 different synthetic concrete slabs, 6 of the slabs have 4 while the rest have 5 perfectly-conducting (PEC) circular-section reinforcing bars inserted, sharing different size and placed at different depth with respect to the surface of slab. These slabs have the same dimension in height and width, which is $0.25m$ and $1m$ respectively, and different dimensions in length, which are $0.7m, 0.9m, 1.1m, 1.3m, 1.5m, 1.7m$ in each slab respectively. Notice the length of the slab decides the number of A-scan measurements per B-scan, this property makes our B-scan dataset have a better versatility which meets the real GPR data collection condition.

Similar to [23], we use Gaussian norm wave as the pulse emitted from GPR in all our simulations, which have a cen-

tral frequency $f_c = 2.4GHz$. The distance between transmitter and receiver of the antenna is set to $5cm$, while time window is $5ns$. The antenna in all simulations is moving along the line orthogonal to the direction we set up the PECs. To match with the commercial GPR data collection frequency, a time sampling measurement is conducted on every consecutive traces with $2mm$. Note that the relative dielectric in all our slabs is set to 7, which matches with the concrete dielectric in real environment. The front view figure of our synthetic slabs is shown in Fig.3.

After the simulations, it generates 628 B-scan data thus our proposed dataset includes these B-scan data which could convert into images, as well as their cross section images as the ground truth.

Sparse Back Projection Aggregation

There are some limitations in the conventional migration process. First of all, it needs to process all A-scan data into back-projected data (which are usually more than thousand) from each GPR B-scan. Moreover, in order to indicate the potential target area, those back-projected data should be overlapped together one by one, which makes the computation too heavier and brings a lot of noise in the output migration image.

Nevertheless, in MigrationNet, we propose a multiple spatial resolution input where the resolution denotes the number of the A-scan measurements to generate back-projected data. Specifically, since each B-scan has different number of A-scan measurements in our dataset, for any B-scan data whose A-scan measurements are less than 1024, 256, 128 and 64 A-scan measurements are selected to be back-projected and stacked in each independent channel as the input, to distinguish the different spatial resolution. Otherwise, for those B-scan data have more than 1024 A-scan signals, we take a sliding-window crop operation on B-scan raw data and separate it into several parts, this operation is equivalent of the Equ.2. Note that the length of sliding-window is fixed to 1024 while the width is as same as the raw B-scan data, which represents the sampling number of an A-scan measurement.

$$m = \lfloor N/1024 \rfloor \tag{2}$$

where N is the number of A-scan measurements in a B-scan and m is the number of cropping B-scans have 1024 A-scans after the trim operation.

By this way, several $M * N * C$ 3D stack input is created, where M demonstrates the number of A-scans in the related B-scan, N indicates the number of the sample data in an A-scan measurement and C is the number of BP data in each stack group.

The reason we choose to sparsely aggregate the back-projected data is that our encoder-decoder based MigrationNet, as will introduce in next section, has a good ability to learn the spatial relationship of the stack input data and could transfer/migrate it into a focused image. Furthermore, this input data with a sparse resolution in spatial domain can not only decrease the computational cost, but also provide a richer input information with multiple resolution in spatial domain. More details will be shown in Section 4.2 and Section 5.1.

4.2. MigrationNet

As shown in Fig.6, our DNN-based migration process contains two steps. First is noise removal process which would filter the raw B-scan data through a segmentation model in order to only keep the hyperbola feature, and stack the filtered 2D data into the 3D form. Then our proposed encoder-decoder network would take the input 3D stack data and output the cross section image corresponding to the raw B-scan image, without implementing *time-zero correction*, *background removal* and *Hilert transformation* operations we demonstrated in Section 3.3.

Noise Removal As introduced in Section 3.1, GPR signal would respond to materials which have different dielectric property so that it is important to us to remove those weak radar responses which caused by noise. Inspired by the related works [11, 27], the details of noise removal are as depicted in Fig.5: 1) by taking advantages of a segmentation model, UNet, we get hyperbolic mask from the input raw B-scan images; 2) we then filter the raw B-scan data with mask B-scan features, the filtered data only keep the strongest response; 3) finally, as demonstrated in Section 4.1, we stack each filtered A-scan signal into back-projected data.

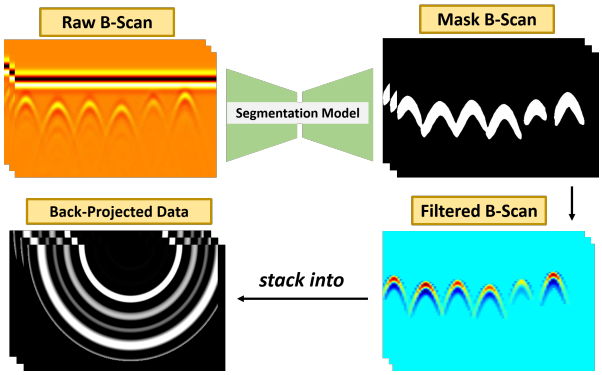

Figure 5. Noise removal process on GPR raw B-scan image. Raw B-scan data is firstly processed by an segmentation model to show the mask area, then the B-scan data get filtered by only keeping the data inside the mask region. At last, the back-projected data is generated from the filtered B-scan and stacked together.

Multiple Spatial Resolution Encoder The encoder takes charge of interpreting the intrinsic information in the input stacked back-projected data as a migration image. Our proposed encoder is an extended version of UNet, it inherits the context capture ability by a spatial down-sampling

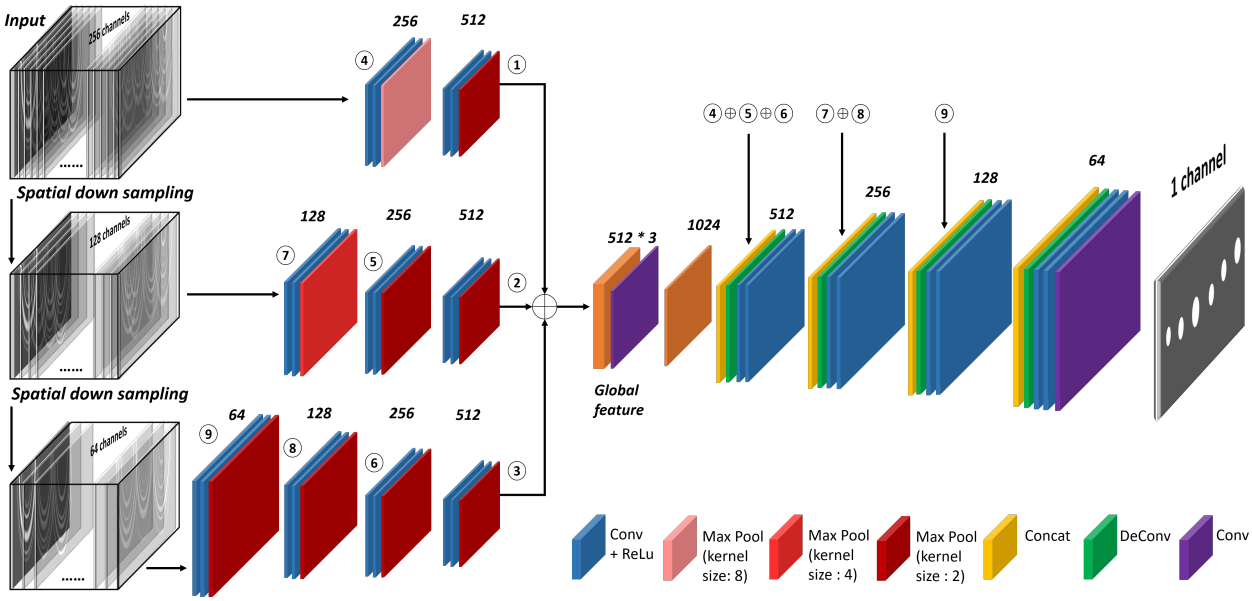

Figure 6. Schematic of the proposed DNN-based migration framework. The input is the stacked BP data with 256 channels, and further down-sampling into 128 and 64 channels in spatial domain. Then, the global features are extracted through the multiple spatial resolution encoder and further concatenated into 1536 channels. The encoder consists of several de-convolutional groups, the global feature is combined with local features from MSRE through skip-connection operation indicated by $\oplus$ while ① to ⑨ present the last layer feature in each de-convolutional group, and finally decoded into a binary migration image.

group, which is a combination of two convolution layers and one max-pooling layer.

We first introduce our feature extractor, named as Multiple Spatial Resolution Encoder (MSRE) while the common feature extractor in most related works [17, 27, 35] take no advantage of resolution information of the input data. As depicts in Fig.6, our input BP data is stacked with different channels to indicate multiple resolution in spatial domain. Thus, our method could make good use of sparse stack BP data, which would reveal the rich local structure information in spatial domain.

Specifically, the multiple input to our encoder is a stacked BP data with 256 channels, 128 channels and 64 channels respectively. In addition, for those B-scan contains more than 1024 A-scans, we crop it and back-projected the A-scans into the stack format as introduced in Section 4.1. Notice those BP data to create the input are selected randomly from B-scan signal, in order to have a better perception to the local feature. These multiple spatial resolution input will be mapped by three independent feature extractor, MSRE, to generate the latent feature.

In MSRE, according to the input data with different channels and spatial resolution, we follow the down-sampling group to encode them into a feature map f with the same size, where size = [M x N x 512]. In details, to get the same size of output feature, the 256 channels dense input data follows a down-sampling group where the kernel size of max-pooling layer is 8. In the meanwhile, for 128 channels input, the kernel size of the first max-pooling layer is 4 while the rest of pooling layers' kernel size are all equal to 2. As 64 channels sparse input, all the kernel size of max-pooling layers in the down-sampling groups are 2 and it allows the final output feature map f has the same size in each input.

At last, all three feature maps are then concatenated together as F, where size = [M x N x 1536]. This design brings the combined latent feature ability to contain better spatial information of the input BP data.

Decoder The decoder takes concatenated global feature map F as input and aims to predict a [M x N x 1] migration binary image, with the white indicates the pipe and the black indicates the back ground.

In details, our decoder consists of 5 up-sampling group, and each group contains two convolutional layers and one deconvolutional layer. Besides, we also take the advantage of skip connections. As illustrated in Fig.6, we concatenate the encoder's layer with decoder's layers of each corresponding group. As for those encoder layers which have multiple resolutions, we first take an average on those feature maps and then concatenate with encoder's layer.

4.3. Loss Design

To constrain the shape and size of the pipe, we develop a joint loss in two-level hierarchy – pixel and structure-level, which is able to capture fine structures with clear boundaries. Our hybrid loss function is composed by following

two terms:

Firstly, since most of the non-destructive testing objects have a round shape cross-section (i.e., rebars, utilities, PVC pipes, etc.) as claimed in Section 4.1, it is crucial for us to compare structure similarity between predicted image and the ground truth in order to maintain the proper size and shape. Thus, inspired by [14, 30, 34], we demonstrate the structure comparison loss between predicted image X and ground truth Y as follows:

$$L_1 = \frac{\sigma_{xy} + C}{\sigma_x \sigma_y + C} \tag{3}$$

note that σ_x and σ_y are the standard deviation as an estimate of the image contrast, C is a constant value while σ_{xy} represents the covariance which is:

$$\sigma_{xy} = \frac{1}{N-1} \sum_{i=1}^{N} (x_i - \mu_x)(y_i - \mu_y) \tag{4}$$

where μ_x and μ_y are mean intensity of the predicted image and ground truth respectively, N is the number of pixels in the image.

The second loss expression is a common cross entropy loss as proposed in [27]

$$L_2 = \sum_{x_i \in \mathscr{M}} w^j(x) log(p(x_{i,j})) \tag{5}$$

where x_i indicates an element in given input while M, $p(x_{i,j})$ is the element x_i probabilistic prediction over class j, and w^j is the weight of each classes.

Finally, our loss function could be illustrated as following:

$$L = \lambda_i L_1 + \lambda_j L_2 \tag{6}$$

where λ_i and λ_j are the weight of cross entropy loss and structure loss which satisfy the relation as $\lambda_i + \lambda_j = 1$.

5. EXPERIMENTAL STUDY

We evaluate our DNN-based migration method on the dataset we prepared in Section 4.1. The effectiveness and robustness of our proposed MigrationNet are discussed in details. All the tests are conducted on a server with Intel Core i9-9900K 3.2GHz CPU, GeForce RTX 2080 Ti GPU, and 32GB RAM.

The weights governing the terms in loss function is set to $\lambda_i = 0.1$ and $\lambda_j = 0.9$, we also use the stochastic gradient descent (SGD), select momentum as 0.9 and weight decay as $1e{-}8$. As for the initial learning rate (LR) and input scale, a comparison under different weight setting is given in Table.1. There are three sets of different initial parameters listed, which might affect the training performance. In this three comparative parameters, we select the input scale and initial learning rate at $(0.25, 5e-6)$, $(0.5, 5e-6)$, $(0.25, 5e-5)$ respectively. By evaluating the average accuracy, average precision, average recall as well as F1 score in training dataset, we could conclude that with a learning rate at $5e-6$ and an input scale 0.25, our model could get a better training performance with a converged final loss at $7.7045e-3$.

Table 1. Initial Parameter Effects To The MigrationNet On training data, *AC*: average accuracy, *AP*: average precision, *AR*: average recall, $F1$: the F-score

	MigrationNet					
	Init Param		Init Param		Init Param	
	Scale	LR	Scale	LR	Scale	LR
	0.25	5e-6	0.5	5e-6	0.25	5e-5
AC	**95.70**		91.44		93.47	
AP	**93.90**		87.79		91.23	
AR	91.41		83.54		**91.46**	
F1	**92.64**		85.61		91.34	

5.1. Ablation Study

How the number of input channels matters?

One interesting topic is that how does the channel of stacked BP data, that is, the number of A-scan measurements in the spatial domain, affects the migration performance. It is known that the more A-scan data used, the better migration result (i.e., sharper, brighter and more focused target point in the energy map achieved, however, it is also computation costly to process such a large amount of data.

To access the effectiveness of our multiple spatial resolution encoder and investigate what would be the best spatial resolution for input data, we conduct this experiment to verify the encoder performance with different resolution of input. Given a raw B-scan data, we extract different number of A-scan measurements to back-project them into stack BP data format with different spatial resolution, such as the sparse input with 64 and 128 channels BP data, semi-sparse input with 128 and 256 channels BP data as well as raw input with all the BP data. In addition, we also provide single resolution input such as 64 channels input, 128 channels input and 256 channels input respectively. We still take mean IOU and pixel accuracy as the evaluation index. The results are summarized in Table.2.

We find that pixel accuracy of our proposed input gains a boost which is between 4% to 9% compared to other input groups with multiple spatial resolution, it also gets a better performance compared with single spatial resolution input, even if the raw input with all A-scan measurements. Notice that when the input channel number decreases to 64, it will beyond the MigrationNet's ability to learn spa-

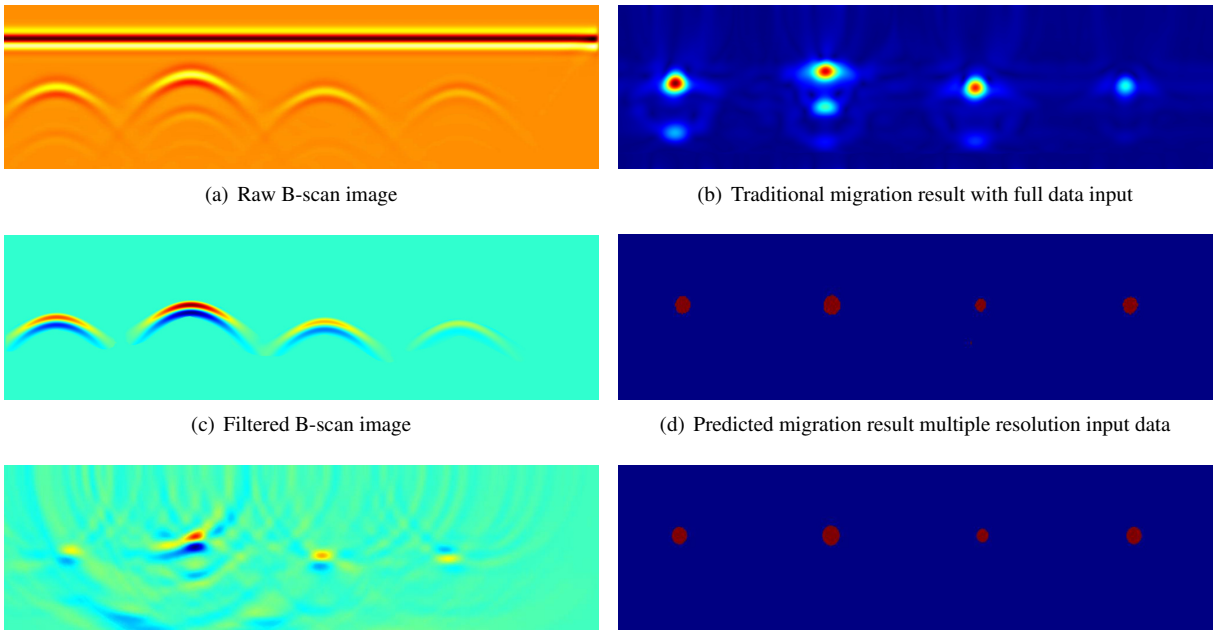

(a) Raw B-scan image

(b) Traditional migration result with full data input

(c) Filtered B-scan image

(d) Predicted migration result multiple resolution input data

(e) Sparse-BP image aggregated in time domain

(f) Ground-Truth of migration result

Figure 7. Migration results comparison between our proposed migration method and conventional migration method.

tial features from such a sparse input. What we expect is that the local geometrical and semantic feature of back-projected data could be better extracted through the combined multi-resolution encoder. The result also indicates that our method has a better understanding of detailed information.

Table 2. Evaluation Performance Comparison with Different Spatial Resolution Input.

Multi-Res. Input Channels	Mean IOU	Pixel Acc%
256+128+64	**89.97**	**95.70**
256+128	83.46	91.31
128+64	66.47	84.29
256	74.95	86.63
128	51.57	76.90
64	-	-
raw	88.64	94.25

How the structure similarity loss matters? To verify the effectiveness of our joint loss, we still make a comparison on the Mean IOU and pixel accuracy, with/without structural similarity loss. As shown in Table.3, our joint loss has a better performance compared with the single Cross Entropy loss, which reveal the fact that this hybrid loss design is able to capture both segmentation information and fine strictures with clear boundaries.

Table 3. Performance Comparison between our joint loss and Cross Entropy loss

	Mean IOU	pixel Acc%
Joint Loss	89.97	95.70
Cross Entropy Loss	87.65	94.65

Table 4. Processing Duration Comparison with Conventional Migration and MigrationNet

	Con. Migration	MigrationNet
Avg. Time Cost (s)	3.47	0.0347

5.2. Effectiveness of MigrationNet

Migration Methods Comparison

As depicted in Fig.7, our proposed method firstly filtered the potential background noise in raw B-scan data, Fig.7 (c) shows the filtered image which kept our ROI area with a highlighted *jetmap* format. Since our back-projected data is stacked into different channels in the spatial domain and thus could not be visualized, in Fig.7 (e), we represented the back-projected data in the time domain which only has one channel, the BP images are displayed with a highlighted *jetmap* format. At last, our predicted migration result, which is illustrated in Fig.7 (d), shows the high performance compared with the traditional migration method.

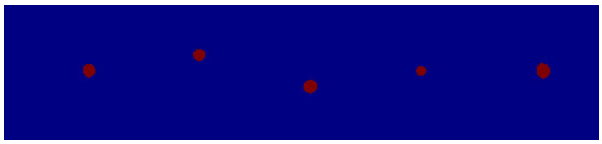

(a) Predicted Migration result with speckle-noised input, noise variance = 0.05

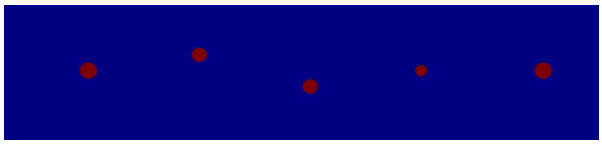

(b) Predicted Migration result without speckle-noised input

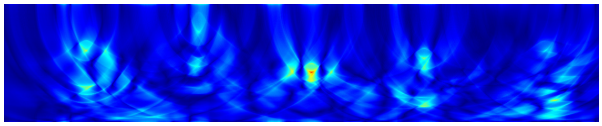

(c) Conventional Migration result with speckle-noised input, noise variance = 0.05

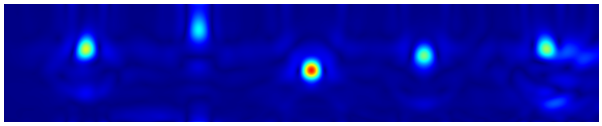

(d) Conventional Migration result without speckle-noised input

Figure 8. Noise Robustness Comparison between conventional and proposed migration method. The subsurface ground truth image is illustrated in Fig.1.

Table 5. Noise Robustness Evaluation Comparison Between Conventional Migration and MigrationNet, root-mean-square error (RMSE) is taken as the evaluation criteria in the following tests.

	Conventional Migration			MigrationNet		
	Gaussian	Salt & Pepper	Speckle	Gaussian	Salt & Pepper	Speckle
Without Noise	37.3491			3.3500		
Variance & Noise density = 0.05	54.3589	51.6030	56.1675	11.4624	11.2508	10.2708
Variance & Noise density = 0.1	62.2094	61.1385	61.8539	17.8093	16.3628	16.0731
Variance & Noise density = 0.2	75.3084	77.7894	76.1743	32.1583	30.9074	29.5939
Variance & Noise density = 0.5	92.4765	90.1059	92.0384	45.3853	42.8437	41.2759

In addition, we also compare the processing time for each single migration process between the conventional method and MigrationNet. The result is shown below in Table.4, which indicates that MigrationNet also gains a boost in computation processing duration due to the heavy computation cost in traditional method.

Noise Robustness

We also tested noise robustness in MigrationNet. In this section, we choose to add *Gaussian white noise*, *salt & pepper noise* and *speckle noise* respectively to the GPR raw data and our stacked 128 channels BP data. We performed 12 sets of experiments on conventional migration method while another 12 sets of experiments on our proposed method. There are 4 different variance and noise density parameters being compared for each of the noise type. The parameter settings are 0.05, 0.1, 0.2 and 0.5 respectively in each of the four tests. After adding different noises respectively to the input for each test, we compared *root-mean-square error (RMSE)* for predicted results between the noised-input and raw data input in proposed method testing, and migration results between noised data input and raw data input in conventional method testing.

As illustrated in Table.5 and Fig.8, we could find our proposed method has a high noise robustness while in conventional method, the noise would significantly influence the migration results.

6. CONCLUSIONS

We have presented a new approach to reveal and localize subsurface pipes or bars in non-destructive testing. To this end, we firstly design a GPR B-scan dataset which matches with both the commercial GPP data collection method and real collecting environment. Then, we process the B-scan data into a stacked 3D format , which provides a better spatial perceptive ability. At last, we propose a encoder-decoder based MigrationNet, which is able to interpret the input stacked data and output the migration result. Our method is effective across multiple spatial resolution input comparison tests. In addition, it shows a good robustness on noise data which would impact conventional migration method extremely. At last, our method could acquire a low cost both in computation and processing time.

7. Acknowledgement and disclaimer

Research was supported in part by NSF Grant No. IIP-1915721, DOT Grant No. 69A3551747126. J. Xiao has significant financial interest in InnovBot LLC, a company involved in R&D and commercialization of the technology.

References

[1] W Al-Nuaimy, Y Huang, M Nakhkash, MTC Fang, VT Nguyen, and A Eriksen. Automatic detection of buried utilities and solid objects with gpr using neural networks and pattern recognition. *Journal of applied Geophysics*, 43(2-4):157–165, 2000.

[2] Maha Almaimani. Classifying gpr images using convolutional neural networks. 2018.

[3] Andrea Benedetto, Francesco Benedetto, and Fabio Tosti. Gpr applications for geotechnical stability of transportation infrastructures. *Nondestructive Testing and Evaluation*, 27(3):253–262, 2012.

[4] Andrea Benedetto, Guido Manacorda, Alessandro Simi, and Fabio Tosti. Novel perspectives in bridges inspection using gpr. *Nondestructive Testing and Evaluation*, 27(3):239–251, 2012.

[5] Lance E Besaw and Philip J Stimac. Deep convolutional neural networks for classifying gpr b-scans. In *Detection and Sensing of Mines, Explosive Objects, and Obscured Targets XX*, volume 9454, page 945413. International Society for Optics and Photonics, 2015.

[6] Norbert Blindow, Sonja K Suckro, Martin Rückamp, Matthias Braun, Marion Schindler, Birgit Breuer, Helmut Saurer, Jefferson C Simões, and Manfred A Lange. Geometry and thermal regime of the king george island ice cap, antarctica, from gpr and gps. *Annals of Glaciology*, 51(55):103–109, 2010.

[7] Jon F Claerbout and Stephen M Doherty. Downward continuation of moveout-corrected seismograms. *Geophysics*, 37(5):741–768, 1972.

[8] David J Daniels. Surface-penetrating radar. *Electronics & Communication Engineering Journal*, 8(4):165–182, 1996.

[9] Sevket Demirci, Enes Yigit, Ismail H Eskidemir, and Caner Ozdemir. Ground penetrating radar imaging of water leaks from buried pipes based on back-projection method. *Ndt & E International*, 47:35–42, 2012.

[10] Mohamed S El-Mahallawy and Mazlan Hashim. Material classification of underground utilities from gpr images using dct-based svm approach. *IEEE Geoscience and Remote Sensing Letters*, 10(6):1542–1546, 2013.

[11] Jinglun Feng, Liang Yang, Haiyan Wang, Yifeng Song, and Jizhong Xiao. Gpr-based subsurface object detection and reconstruction using random motion and depthnet. In *2020 IEEE International Conference on Robotics and Automation (ICRA)*, pages 7035–7041. IEEE, 2020.

[12] Jenö Gazdag. Wave equation migration with the phase-shift method. *Geophysics*, 43(7):1342–1351, 1978.

[13] Fabio Giovanneschi, Kumar Vijay Mishra, Maria Antonia Gonzalez-Huici, Yonina C Eldar, and Joachim HG Ender. Dictionary learning for adaptive gpr landmine classification. *IEEE Transactions on Geoscience and Remote Sensing*, 57(12):10036–10055, 2019.

[14] Clément Godard, Oisin Mac Aodha, and Gabriel J Brostow. Unsupervised monocular depth estimation with left-right consistency. In *Proceedings of the IEEE Conference on Computer Vision and Pattern Recognition*, pages 270–279, 2017.

[15] Mark Grasmueck. 3-d ground-penetrating radar applied to fracture imaging in gneiss. *Geophysics*, 61(4):1050–1064, 1996.

[16] Mark Grasmueck, Ralf Weger, and Heinrich Horstmeyer. Full-resolution 3d gpr imaging. *Geophysics*, 70(1):K12–K19, 2005.

[17] Huimin Huang, Lanfen Lin, Ruofeng Tong, Hongjie Hu, Qiaowei Zhang, Yutaro Iwamoto, Xianhua Han, Yen-Wei Chen, and Jian Wu. Unet 3+: A full-scale connected unet for medical image segmentation. In *ICASSP 2020-2020 IEEE International Conference on Acoustics, Speech and Signal Processing (ICASSP)*, pages 1055–1059. IEEE, 2020.

[18] Wallace Wai-Lok Lai, Xavier Derobert, and Peter Annan. A review of ground penetrating radar application in civil engineering: A 30-year journey from locating and testing to imaging and diagnosis. *Ndt & E International*, 96:58–78, 2018.

[19] Silvia Lameri, Federico Lombardi, Paolo Bestagini, Maurizio Lualdi, and Stefano Tubaro. Landmine detection from gpr data using convolutional neural networks. In *2017 25th European Signal Processing Conference (EUSIPCO)*, pages 508–512. IEEE, 2017.

[20] Wentai Lei, Feifei Hou, Jingchun Xi, Qianying Tan, Mengdi Xu, Xinyue Jiang, Gengye Liu, and Qingyuan Gu. Automatic hyperbola detection and fitting in gpr b-scan image. *Automation in Construction*, 106:102839, 2019.

[21] J Les Davis, James R Rossiter, E Darel, and Cece B Dawley. Quantitative measurement of pavement structures using radar. In *Fifth International Conferention on Ground Penetrating Radar*, 1994.

[22] Haifeng Li, Chieh Chou, Longfei Fan, Binbin Li, Di Wang, and Dezhen Song. Toward automatic subsurface pipeline mapping by fusing a ground-penetrating radar and a camera. *IEEE Transactions on Automation Science and Engineering*, 17(2):722–734, 2019.

[23] Simone Meschino and Lara Pajewski. Spot-gpr: A freeware toolfor target detection and localizationin gpr data developedwithin the cost action tu1208. *Journal of Telecommunications and Information Technology*, 2017.

[24] Caner Özdemir, Şevket Demirci, Enes Yiğit, and Betül Yilmaz. A review on migration methods in b-scan ground penetrating radar imaging. *Mathematical Problems in Engineering*, 2014, 2014.

[25] Umut Ozkaya, Farid Melgani, Mesay Belete Bejiga, Levent Seyfi, and Massimo Donelli. Gpr b scan image analysis with deep learning methods. *Measurement*, page 107770, 2020.

[26] Minh-Tan Pham and Sébastien Lefèvre. Buried object detection from b-scan ground penetrating radar data using faster-rcnn. In *IGARSS 2018-2018 IEEE International Geoscience and Remote Sensing Symposium*, pages 6804–6807. IEEE, 2018.

[27] Olaf Ronneberger, Philipp Fischer, and Thomas Brox. U-net: Convolutional networks for biomedical image segmentation. In *International Conference on Medical image computing and computer-assisted intervention*, pages 234–241. Springer, 2015.

[28] William A Schneider. Integral formulation for migration in two and three dimensions. *Geophysics*, 43(1):49–76, 1978.

[29] Stefano Urbini, Luca Vittuari, Stefano Gandolfi, et al. Gpr and gps data integration: examples of application in antarctica. 2001.

[30] Zhou Wang, Alan C Bovik, Hamid R Sheikh, and Eero P Simoncelli. Image quality assessment: from error visibility to structural similarity. *IEEE transactions on image processing*, 13(4):600–612, 2004.

[31] Craig Warren, Antonios Giannopoulos, and Iraklis Giannakis. gprmax: Open source software to simulate electromagnetic wave propagation for ground penetrating radar. *Computer Physics Communications*, 209:163–170, 2016.

[32] Zhongming Xiang, Abbas Rashidi, and Ge Ou. An improved convolutional neural network system for automatically detecting rebar in gpr data. *arXiv preprint arXiv:1907.09997*, 2019.

[33] Xinjun Xu, Yang Lei, and Feng Yang. Railway subgrade defect automatic recognition method based on improved faster r-cnn. *Scientific Programming*, 2018, 2018.

[34] Hang Zhao, Orazio Gallo, Iuri Frosio, and Jan Kautz. Loss functions for neural networks for image processing. *arXiv preprint arXiv:1511.08861*, 2015.

[35] Zongwei Zhou, Md Mahfuzur Rahman Siddiquee, Nima Tajbakhsh, and Jianming Liang. Unet++: A nested u-net architecture for medical image segmentation. In *Deep Learning in Medical Image Analysis and Multimodal Learning for Clinical Decision Support*, pages 3–11. Springer, 2018.